Monthly Notices
of the
ROYAL ASTRONOMICAL SOCIETY

MNRAS **465,** 4375–4380 (2017)
Advance Access publication 2016 November 22

doi:10.1093/mnras/stw2993

Constraining stellar binary black hole formation scenarios with *eLISA* eccentricity measurements

Atsushi Nishizawa,[1]★ Alberto Sesana,[2] Emanuele Berti[1,3]★ and Antoine Klein[1,3]

[1]*Department of Physics and Astronomy, The University of Mississippi, University, MS 38677, USA*
[2]*School of Physics and Astronomy, University of Birmingham, Edgbaston, Birmingham B15 2TT, United Kingdom*
[3]*CENTRA, Departamento de Física, Instituto Superior Técnico, Universidade de Lisboa, Avenida Rovisco Pais 1, P-1049 Lisboa, Portugal*

Accepted 2016 November 15. Received 2016 November 14; in original form 2016 June 29

ABSTRACT

A space-based interferometer such as the *evolved Laser Interferometer Space Antenna* (*eLISA*) could observe a few to a few thousands of progenitors of black hole binaries (BHBs) similar to those recently detected by Advanced LIGO. Gravitational radiation circularizes the orbit during inspiral, but some BHBs retain a measurable eccentricity at the low frequencies where *eLISA* is the most sensitive. The eccentricity of a BHB carries precious information about its formation channel: BHBs formed in the field, in globular clusters, or close to a massive black hole (MBH) have distinct eccentricity distributions in the *eLISA* band. We generate mock *eLISA* observations, folding in measurement errors, and using a Bayesian model selection, we study whether *eLISA* measurements can identify the BHB formation channel. We find that a handful of observations would suffice to tell whether BHBs were formed in the gravitational field of an MBH. Conversely, several tens of observations are needed to tell apart field formation from globular cluster formation. A 5-yr *eLISA* mission with the longest possible armlength is desirable to shed light on BHB formation scenarios.

Key words: black hole physics – gravitational waves.

1 INTRODUCTION

The first direct observation of merging black hole binaries (BHBs) during the first observation run (O1) of Advanced LIGO marked a milestone in the history of astronomy and fundamental physics. The observation of two events (GW150914 and GW151226), plus a third candidate LVT151012 (Abbott et al. 2016a,b,d), provides a formidable laboratory to test general relativity in the strong-gravity regime (Abbott et al. 2016e). In addition, gravitational-wave observations of BHBs can further our understanding of their astrophysical formation channels (Abbott et al. 2016f). Different formation scenarios result in distinct BHB binary properties, which may be disentangled by analysing the statistical parameters of a sufficiently large number of detections. The currently favoured scenarios involve the stellar evolution of field binaries (Postnov & Yungelson 2014) and the dynamical capture of BHs in globular clusters (Benacquista & Downing 2013). Recent work showed that both field formation (Mapelli, Colpi & Zampieri 2009; Belczynski et al. 2010; Dominik et al. 2012, 2013, 2015; Spera, Mapelli & Bressan 2015; Belczynski et al. 2016a,b) and cluster formation (Rodriguez et al. 2015a; Chatterjee, Rodriguez & Rasio 2016; Rodriguez, Chatterjee & Rasio 2016a; Rodriguez et al. 2016b) are compatible with the recent Advanced LIGO observations (Abbott et al. 2016f). More exotic proposals include the formation via hierarchical triples (Wen 2003; Antonini, Murray & Mikkola 2014; Antonini et al. 2016), a Population III origin for the binary members (Kinugawa et al. 2014; Hartwig et al. 2016), chemically homogeneous evolution in short-period binaries (Mandel & de Mink 2016; de Mink & Mandel 2016; Marchant et al. 2016) and even primordial BHs (Bird et al. 2016).

In the field formation scenario, BHBs have very small eccentricities in the Advanced LIGO band, and the BH spins could be preferentially aligned with the orbital angular momentum as a consequence of mass-transfer episodes preceding the stellar collapse. In the globular cluster scenario, BHBs are formed via dynamical processes (involving mostly three- and four-body encounters), generally resulting in highly eccentric orbits (see e.g. Rodriguez et al. 2016a). Moreover, as a consequence of the chaotic nature of the BHB formation process, the spins of the two BHs are likely to be randomly oriented. Earth-based gravitational-wave observations could potentially differentiate between field and cluster formation by looking at mass, mass ratio and possibly redshift distributions (Rodriguez et al. 2015b), as well as spin dynamics. As for the latter, however, one should consider that the details of mass transfer and tidal alignment in BH binaries, as well as the degree of asymmetry in stellar collapse – and the resulting kicks imparted to the BHs – are quite uncertain, and they will affect BH spin alignment and gravitational waveforms in complex ways (Belczynski et al. 2008; Gerosa et al. 2013; Gerosa et al. 2015; Belczynski et al. 2016a).

★ E-mail: anishiza@olemiss.edu (AN); eberti@olemiss.edu (EB)

In this respect, eccentricity may be a complementary robust tracer of the formation channel. In addition, a characteristic eccentricity distribution can be a tracer of a formation scenario even for primordial BHs (Cholis et al. 2016). Radiation reaction is well known to circularize the orbit. While field and cluster formation scenarios predict very distinct eccentricity distributions at BHB formation, both scenarios result in nearly circular binaries in the Advanced LIGO band. The first observed signals did not set strong bounds on the eccentricity of the binary (Abbott et al. 2016b,c), and it is quite unlikely that eccentricity measurements with ground-based detectors will ever differentiate between the field and cluster scenarios. However, Sesana (2016) showed that, depending on the intrinsic rates (which are only loosely constrained by current detections) and on the detector baseline, the *evolved Laser Interferometer Space Antenna* (*eLISA*) will observe a few to a few thousands of BHBs (see also Kyutoku & Seto 2016). Because of the much lower frequency band, *eLISA* will detect these systems *before* circularization, and in many cases, it will be able to measure their eccentricity (Nishizawa et al. 2016).

In this article, we use a Bayesian model selection to demonstrate how *eLISA* eccentricity measurements can conclusively distinguish between different BHB formation channels. In Section 2, we consider three models for BHB formation, and discuss the eccentricity distributions predicted by these models in the *eLISA* band.[1] In Section 3, we simulate and analyse *eLISA* observations using various models and detector baselines. In Section 4, we present our main results, and in Section 5, we discuss their implications. We assume a concordance Λ cold dark matter cosmology with $h = 0.679$, $\Omega_{\rm M} = 0.306$ and $\Omega_\Lambda = 0.694$ (Planck Collaboration XIII 2015).

2 ASTROPHYSICAL MODELS AND ECCENTRICITY DISTRIBUTIONS

We consider a BHB population merging at a rate $\mathcal{R}$, characterized by a chirp mass probability distribution $p(\mathcal{M}_{\rm r})$ – where $\mathcal{M}_{\rm r} \equiv (M_{1,{\rm r}} M_{2,{\rm r}})^{3/5}/(M_{1,{\rm r}} + M_{2,{\rm r}})^{1/5}$, and a subscript 'r' denotes quantities in the rest frame of the source – and by an eccentricity probability distribution $p(e_*)$ at some reference frequency f_* close to coalescence (we set $f_* = 10$ Hz). If $p(e_*)$ depends only on the BHB formation route, but not on the chirp mass and redshift, the merger rate density per unit mass and eccentricity is given by

$$\frac{{\rm d}^3 n}{{\rm d}\mathcal{M}_r {\rm d}t_{\rm r} {\rm d}e_*} = p(\mathcal{M}_{\rm r})\, p(e_*)\, \mathcal{R}. \tag{1}$$

Equation (1) can then be converted into a number of sources emitting per unit mass, redshift and frequency at any time via

$$\frac{{\rm d}^4 N}{{\rm d}\mathcal{M}_{\rm r} {\rm d}z {\rm d}f_{\rm r} {\rm d}e_*} = \frac{{\rm d}^3 n}{{\rm d}\mathcal{M}_{\rm r} {\rm d}t_{\rm r} {\rm d}e_*} \frac{{\rm d}V}{{\rm d}z} \frac{{\rm d}t_{\rm r}}{{\rm d}f_{\rm r}}(e(e_*, f)), \tag{2}$$

where ${\rm d}V/{\rm d}z$ is the standard volume shell per unit redshift, and

$$\frac{{\rm d}t_{\rm r}}{{\rm d}f_{\rm r}}(e(e_*, f)) = \frac{5c^5}{96\pi^{8/3}} (G\mathcal{M}_{\rm r})^{-5/3} f_{\rm r}^{-11/3} \frac{1}{F(e(e_*, f))}. \tag{3}$$

Here,

$$F(e(e_*, f)) = (1 - e^2)^{-7/2} \left(1 + \frac{73}{24} e^2 + \frac{37}{96} e^4\right), \tag{4}$$

and $e(e_*, f)$ is computed by finding the root of

$$\frac{f}{f_*} = \left[\frac{1 - e_*^2}{1 - e^2} \left(\frac{e}{e_*}\right)^{12/19} \left(\frac{1 + \frac{121}{304} e^2}{1 + \frac{121}{304} e_*^2}\right)^{870/2299}\right]^{-3/2}. \tag{5}$$

We can construct a population of systems potentially observable by *eLISA* by Monte Carlo sampling from the distribution in equation (2) using appropriate distribution functions for $p(\mathcal{M}_{\rm r})$ and $p(e_*)$. For the mass distribution, we employ the 'flat' mass function of Abbott et al. (2016f), i.e. we assume that the two BH masses are independently drawn from a log-flat distribution in the range of $5 < M_{1,2,{\rm r}} < 100\,{\rm M}_\odot$, restricting the total BHB mass to be less than $100\,{\rm M}_\odot$.[2]

For the eccentricity distribution, we consider, as a proof of concept, three popular BHB formation scenarios:

(i) Model *field*: This is the default BHB field formation scenario of Kowalska et al. (2011), taken to be representative of BHBs resulting from stellar evolution.

(ii) Model *cluster*: Globular clusters efficiently form BHBs via dynamical capture. Most of these BHBs are ejected from the cluster and evolve in isolation until they eventually merge. Because of their dynamical nature, BHBs typically form with a thermal eccentricity distribution. A comprehensive study of this scenario has been performed by Rodriguez et al. (2016a).

(iii) Model *MBH*: BHs and BHBs are expected to cluster in galactic nuclei because of strong mass segregation. In this case, binaries within the sphere of influence of the central MBH undergo Kozai–Lidov resonances, forming triplets in which the external perturber is the MBH itself. This scenario has been investigated in Antonini & Perets (2012), and it results in high BHB eccentricities.

The proponents of all models listed above conveniently evolved the BHB populations close to the merger, constructing the resulting eccentricity distributions at a fixed frequency. In more detail, the three distributions we adopt are as follows:

(i) the fiducial model shown in fig. 5 of Kowalska et al. (2011) at $f = 3$ Hz for the *field* scenario (smoothed out and extrapolated to $f_* = 10$ Hz);

(ii) the one shown in fig. 10 of Rodriguez et al. (2016a) at $f_* = 10$ Hz for the *cluster* scenario; and

(iii) the 'cusp model' shown in fig. 7 of Antonini & Perets (2012) at $f_* = 10$ Hz for the *MBH* scenario. Those are shown in the top panel of Fig. 1 and are the starting point of our eccentricity distribution reconstruction. In the bottom panel, assuming that the eccentricity evolves exclusively through gravitational wave emission, we propagate these distributions 'back in time' to obtain $p(e_0)$ at a frequency $f_0 = 0.01$ Hz, where most *eLISA* detections are expected to occur. In this calculation, we must take into account the fact that highly eccentric binaries evolve more quickly – by a factor of $F(e)$ – than circular ones so that only a few highly eccentric binaries will be observable in the *eLISA* band for a given coalescence rate.

[1] For a detailed astrophysical comparison of BHBs formed in galactic fields and globular clusters observable by *eLISA*, see Breivik et al. (2016).

[2] Although this choice results in a BHB population biased towards heavy systems, we found that this does not affect the properties of the *eLISA*-detected systems. In fact, a heavy-biased mass function implies a low intrinsic coalescence rate, for consistency with Advanced LIGO measurements (see fig. 10 in Abbott et al. 2016b). Assuming a more conservative Salpeter mass function results in a comparable number of *eLISA* detections, by virtue of the higher intrinsic rate.

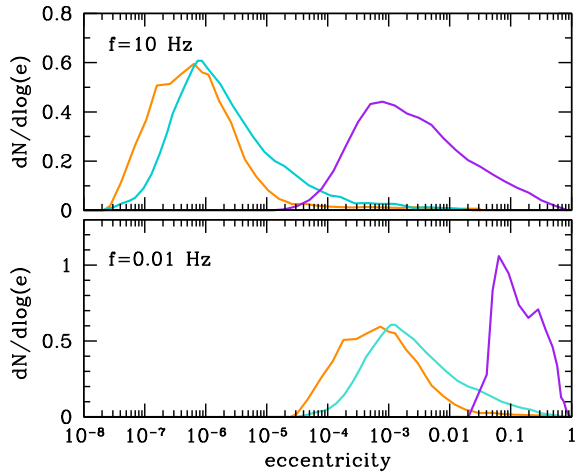

Figure 1. Eccentricity distributions predicted by the *field* (orange), *cluster* (turquoise) and *MBH* (purple) scenarios. The top panel shows the distribution at the reference frequency $f_* = 10$ Hz, while the bottom panel is the observable distribution $p(e_0)$ evolved 'back in time' to $f_0 = 0.01$Hz.

3 SIMULATIONS AND ANALYSIS TOOLS

We consider two *eLISA* baselines, N2A2 and N2A5, in the notation of Klein et al. (2016). We adopt the noise level (N2) recently demonstrated by *LISA Pathfinder* (Armano et al. 2016), and, following the recommendations of the GOAT committee,[3] we choose armlengths of two (A2) and five (A5) million kilometres. We also explore two nominal mission lifetimes (2 and 5 yr) for a total of four mission baselines: N2A2-2y, N2A2-5y, N2A5-2y and N2A5-5y.

For our simulated experiments, we need (i) the *theoretical* eccentricity distribution $\mathcal{P}_X(e_0)$ predicted by the three BHB formation models, and (ii) catalogues of 'synthetic' *eLISA* observations to be tested against the models. The theoretical distributions are generated as follows:

(i) Following the formalism described in Section 2, for each model we generate a large Monte Carlo catalogue of BHBs emitting in the *eLISA* frequency window.

(ii) For each *eLISA* baseline, we select a sample of 10^4 detectable BHBs with a signal-to-noise ratio (S/N) > 8 and construct an histogram of $\mathcal{P}_X(e_i)$ on a grid of logarithmically spaced bins $\Delta(\log\, e_i) = 0.1$ centred at eccentricity values e_i.

(iii) We fit a smooth 10th-order polynomial function to the set of points $(e_i, \mathcal{P}_X(e_i))$, which is generally accurate at a 0.003 level.

This procedure yields 12 *theoretical* eccentricity distributions to be tested against observations for each setup (i.e. for each combination of BHB formation model and *eLISA* baseline).

The next step is the generation of synthetic BHB observations. We use the Fourier-domain eccentric waveforms by Tanay, Haney & Gopakumar (2016) in the small-eccentricity approximation, which is accurate up to (Newtonian, e_0^6) order in amplitude and (2PN, e_0^6) order in phase. The non-spinning eccentric waveforms have 10 physical parameters $\{\mathcal{M}_z, \eta, t_c, \phi_c, D_L, e_0, \bar{\theta}_L, \bar{\phi}_L, \bar{\theta}_S, \bar{\phi}_S\}$: redshifted chirp mass, symmetric mass ratio, time and phase at coalescence, luminosity distance, eccentricity at 10^{-2} Hz, two angles describing the direction of the orbital angular momentum and two angles corresponding to the orientation of the source in the sky. We select 10^3 detectable events with S/N > 8 (because of computational limitations) and with an eccentricity smaller than 0.1 when *eLISA* observations begin (because of limitations in our waveform model, that becomes unreliable for high eccentricities). For each of these events, we compute the error Δe_0 in the measurement of the binary eccentricity e_0 using the Fisher information matrix, as described in Nishizawa et al. (2016).[4] For any given number $1 \leq N_{\rm obs} \leq 100$ of observed BHBs with S/N > 8, depending on the *eLISA* configuration and BHB merger rate, we draw 100 random catalogues of $N_{\rm obs}$ systems from the 10^3 simulated detections.

[3] http://www.cosmos.esa.int/web/goat

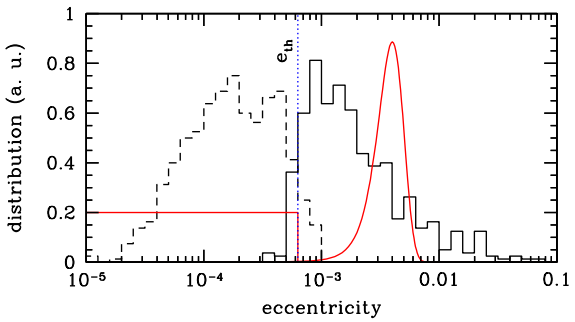

Figure 2. Distribution of BHBs with $\Delta e_0 < e_0$ (solid histogram) and with $\Delta e_0 > e_0$ (dashed histogram), assuming the *field* formation channel and the N2A5-5yr baseline. The dashed blue vertical line marks $e_{\rm th} \approx 6 \times 10^{-4}$. Two examples of $p(e_0)$ are shown in red: a Gaussian distribution for a case with measured eccentricity (right-hand side) and a step-function (log-flat) distribution for an upper limit (left-hand side). The y-axes are in arbitrary units.

As shown by Nishizawa et al. (2016), *eLISA* will enable precise measurements of e_0 down to $e_0 \approx 10^{-3}$, with a mild dependence on armlength or observation time. Roughly speaking, as shown in Fig. 2, this means that e_0 can be measured above some threshold $e_{\rm th}$. To fold in error measurements into each catalogue, we split the events into two classes: (i) If $\Delta e_0 < e_0$, the eccentricity is measurable, and we assign to the eccentricity a probability distribution $p(e_0) = 1/\sqrt{2\pi\Delta e_0^2} \times \exp[-(e_0 - \bar{e})^2/(2\Delta e_0^2)]$, where the measured value $\bar{e}$ is drawn from a Gaussian distribution centred on e_0 with variance Δe_0. (ii) If $\Delta e_0 > e_0$, we simply assume that we have an upper limit on e_0, which we take to be $e_{\rm th}$ for simplicity. The probability distribution is then constructed to be flat in log space in a range of $e_{\rm min} < e_0 < e_{\rm th}$, i.e. $p(\log e_0) = 1/(\log e_{\rm th} - \log e_{\rm min})$. We caution that these assumptions carry a certain degree of arbitrariness. In case (i), $p(e_0)$ extends to negative values when the condition $\Delta e_0 \ll e_0$ is broken, which is the case when $e_0 \gtrsim e_{\rm th}$. When this occurred, we simply ignored the negative part of the distribution. In case (ii), instead, we have the freedom to pick $e_{\rm min}$, which we fix to be 10^{-7}. We verified (for example, by trying different values of $e_{\rm min}$) that neither of these choices affects our results. Examples of eccentricity probability distributions are shown in Fig. 2.

For each setup and each $N_{\rm obs}$, this procedure yields 100 catalogues of observed events, each characterized by the appropriate $p(e_0)$. The 100 catalogues are not independent when $N_{\rm obs} > 10$, since most of them will share some events. However, even for the 'shared' events, $\bar{e}$ is obtained from a different random draw each time, and therefore $p(e_0)$ is different in different catalogues. We checked that the results presented in the next section are unaffected when we consider a smaller number of truly independent catalogues (e.g. 10 catalogues

[4] We refer the reader to section V-D of Nishizawa et al. (2016) for a critical discussion of the appropriateness of the Fisher matrix approximation in this context.

with $N_{\rm obs} = 100$). We are therefore confident that our results are robust with respect to statistical fluctuations.

3.1 Statistical analysis

For a given *eLISA* baseline, our main goal is to consider catalogues of $N_{\rm obs}$ observed events from model A (chosen among *field*, *cluster* and *MBH*) and assess to what confidence (if any) we can say whether the underlying astrophysical model was in fact A, or an alternative model B. This is a classic Bayesian model selection problem. To compare two models A and B, we must compute the odds ratio as follows:

$$O_{AB} = \frac{\mathcal{Z}_A P(A)}{\mathcal{Z}_B P(B)}, \tag{6}$$

where $\mathcal{Z}_X$ is the evidence of model X and $P(X)$ is the prior belief that model X is right. In the absence of prior information, we conservatively assume $P(A) = P(B) = 0.5$. Moreover, for non-parametric models (i.e. models without free parameters, as those considered here), the evidence is simply the likelihood $P(D|X)$ of the data, given the model. The odds ratio then reduces to the likelihood ratio

$$O_{AB} = \frac{P(D|A)}{P(D|B)}. \tag{7}$$

In our case, for each set of $N_{\rm obs}$ measurements, we have $i = 1, \ldots, N_{\rm obs}$ probability distributions of measured eccentricity $p_i(e_0)$ to be compared with the theoretical eccentricity distribution predicted by a given model, $\mathcal{P}_X(e_0)$. Strictly speaking, $N_{\rm obs}$ also depends on eccentricity because eccentricity affects the detectability of the signal. However, we can neglect this dependence because in the small-eccentricity approximation, the S/N is modified by terms of order $\mathcal{O}(e_0^2)$, with corrections that are typically 1 per cent. The likelihood of the data given the model is therefore given by

$$P(D|X) = \prod_{i=1}^{N_{\rm obs}} \int p_i(e_0)\mathcal{P}_X(e_0){\rm d}e_0. \tag{8}$$

In this framework, we can also assign to model A a probability $p_A = P(D|A)/[P(D|A) + P(D|B)]$ and to model B the complementary probability $p_B = 1 - p_A$. From equation (7), $p_A = O_{AB}/(O_{AB} + 1)$. It is therefore natural to associate the odds ratio with the 'confidence' in a given model. For example, if $O_{AB} \simeq 20$, then $p_A \simeq 0.95$, and we can say that model A is favoured at 2σ (95 per cent confidence). Definitive 5σ identification can be associated with $O_{AB} \sim 10^6$.

For each of the 100 catalogues of $N_{\rm obs}$ detections, generated for each setup, we compute the likelihood of the observed data against each model: *field*, *cluster* and *MBH*. If the observations can discriminate between different models, the odds ratio will favour the actual model from which the data were drawn. For each comparison, we then compute the probabilities p_A and p_B defined above, which describe our degree of confidence that the data were actually drawn from either of the models considered in the comparison.

4 RESULTS

In Fig. 3, we compare the median $\log(O_{AB})$ as a function of $N_{\rm obs}$ for each pair of models. The median is computed over 100 Monte Carlo catalogues for each value of $N_{\rm obs}$. The two lower panels show that, regardless of the detector baseline, model *MBH* can be confidently separated – with $\log(O) = 6$, i.e. at approximately 5σ – from any other model after a handful of observations. This is because the eccentricity distribution for model *MBH* is biased towards high

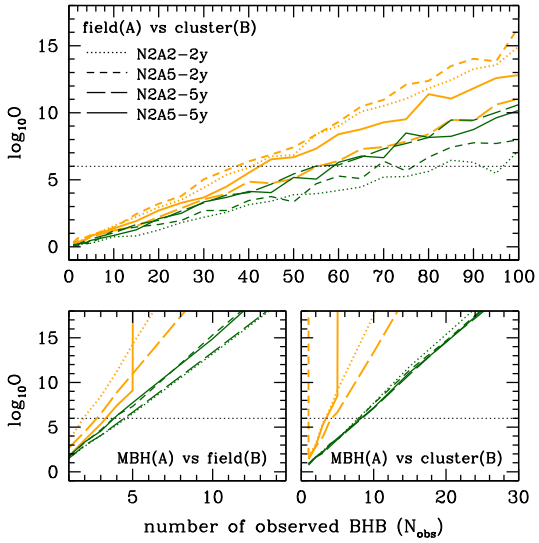

Figure 3. Median odds ratio as a function of $N_{\rm obs}$ for different model pairs and different detector baselines, as labelled in the figure. In each comparison, thick orange curves represent O_{AB} when A is the true model, whereas thin green curves represent O_{BA} when B is the true model.

values (see Fig. 1), at variance with other models. Note also that it is easier to reject model *MBH* when it is false (orange curves) than to confirm it when it is true (green curves). This is because models *field* and *cluster* allow for low eccentricities that are not supported by model *MBH* (Fig. 1). As soon as a BHB has a measured eccentricity $e_0 < 0.01$, model *MBH* is automatically rejected. The converse is not true: The eccentricity range of model *MBH* is also supported by the other models. Therefore, when BHB formation is indeed described by model *MBH*, there is always a chance that highly eccentric BHBs were drawn from other models, and a few more detections are required to reject them. Models *field* and *cluster*, on the other hand, predict similar eccentricity distributions. Depending on which one was the true model and on the *eLISA* baseline, a number of detections between 30 and 95 are needed to achieve the $\log(O) = 6$ threshold.

Since all detector baselines yield similar results, we take a closer look at the N2A2-5y case, a plausible 'minimum' *eLISA* baseline target. In Fig. 4, we show odds ratios for this specific configuration, including the 90 per cent confidence interval computed from the 100 catalogues constructed for each $N_{\rm obs}$. The $\log(O) = 6$ threshold is always achieved with less than 10 observed BHBs when the *MBH* model is involved in the comparison, whereas up to 100 BHBs may be needed to discriminate between the *field* and *cluster* models, depending on the specific ensemble of observed BHBs.

When comparing two models A and B for a given *eLISA* baseline, we can use the 100 catalogues at a fixed $N_{\rm obs}$ to construct cumulative distributions functions (CDFs) of p_A and p_B (Sesana et al. 2011). Suppose that, in a comparison between models A and B, A is the right model, and we draw 100 realizations of $N_{\rm obs}$ observations from model A. We can compute the associated CDF of p_A and plot it against the confidence ($0 < p < 1$). The result for different values of $N_{\rm obs}$ is shown in the upper curves of each panel of Fig. 5. We can also draw 100 realizations of $N_{\rm obs}$ observations from B and compute the CDF of p_A when A is not true. The result are the lower curves in each panel of Fig. 5.

Set, for example, $p = 0.95$ (approximately 2σ). The value of the upper curve at p is the fraction of realizations for which we have more than 2σ confidence that model A is correct when it is, in

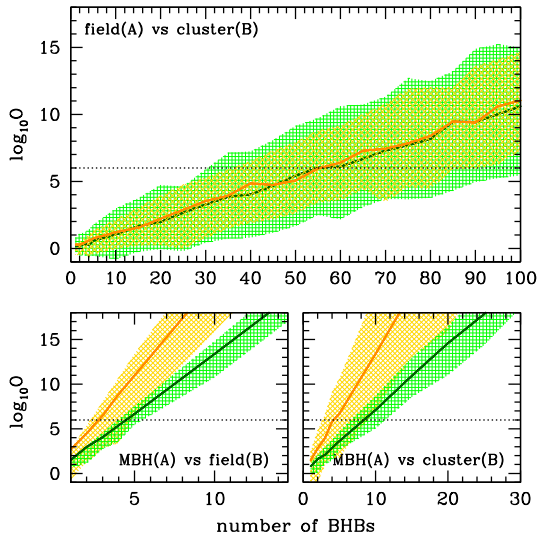

Figure 4. Median and 90 per cent confidence interval of the odds ratio as a function of $N_{\rm obs}$ for baseline N2A2-5y. For each value of $N_{\rm obs}$, we consider 100 Monte Carlo realizations. In each comparison panel, orange curves and shaded areas represent O_{AB} when A is the true model, whereas green curves represent O_{BA} when B is the true model.

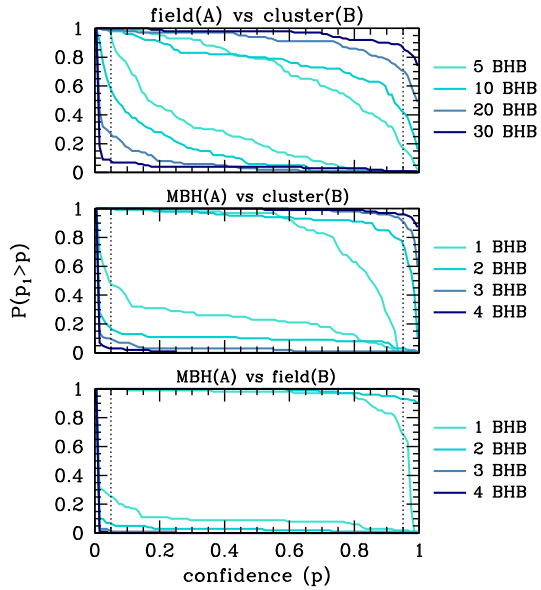

Figure 5. CDF of the confidence in a given model over 100 Monte Carlo realizations of the observed BHB sample for different BHB observations $N_{\rm obs}$ (as labelled in each panel) assuming the N2A2-5y *eLISA* baseline. The top curve in each pair marks the CDF of confidence in model A when model A is true, whereas the bottom curve marks the CDF of confidence in model A when model B is true.

fact, true. The value of the lower curve at $1 - p$ is the fraction of realization for which we cannot rule out model A at 2σ confidence when it is the wrong model (i.e. observations are generated by model B). Fig. 5 presents a similar analysis for all pairs of models assuming the N2A2-5y baseline. About 30 BHB observations are required for a 2σ-confidence identification of model *field* against model *cluster* in about 90 per cent of the realizations. The same level of confidence requires only four and two BHBs when model *MBH* is compared with models *cluster* and *field*, respectively.

Table 1. Expected number of sources (column 2) for each *eLISA* baseline (column 1), compared with the number of observations needed to distinguish between models *field* and *cluster* at a given confidence threshold in 50 per cent (N_{50}) and 90 per cent (N_{90}) of the cases (columns 3–6).

		3σ		5σ	
eLISA base	$N_{\rm obs}$	N_{50}	N_{90}	N_{50}	N_{90}
N2A2-2y	10–80	35	>100	95	>100
N2A5-2y	80–600	34	95	80	>100
N2A2-5y	50–300	25	60	61	100
N2A5-5y	300–2500	25	62	60	100

5 DISCUSSION AND OUTLOOK

For the log-flat distribution assumed here, the Advanced LIGO observations imply a 90 per cent credible interval for the merger rate of $\mathcal{R} = [10, 70]$ yr^{-1} Gpc^{-3} (Abbott et al. 2016b). The resulting range in $N_{\rm obs}$ is reported in Table 1 for the different baselines, and it should be compared with the number of events needed to discriminate among different models at a desired confidence threshold. Model *MBH* can be identified by all the configurations with just a few BHB observations; therefore, it is not reported in the table. Discriminating between the *cluster* and *field* scenarios requires tens of events, and only the baseline N2A5-5y can guarantee a 5σ confidence with 90 per cent probability. Baselines N2A2-5y and N2A5-2y can distinguish among these models at the 3σ level, but this may not be possible should the event rate lean towards the lower limit of the allowed range. The N2A2-2y baseline performs relatively poorly, and it may not deliver enough detections to pin down the formation mechanism.

These results highlight the importance of aiming for a 5-yr mission with the longest possible armlength. However, we should bear in mind some limitations of our proof-of-principle analysis. First of all, we selected three representative models from the literature: This does not fully capture all of the relevant physics affecting the eccentricity distribution of BHBs. For example, several variations of the 'fiducial' model of Kowalska et al. (2011) result in slightly different eccentricity distributions. Our analysis can be applied systematically to any such variation, assessing to what extent the underlying physics can be constrained. Secondly, we assumed the eccentricity distribution to be independent of masses and redshifts. In practice, different formation channels will result in different mass–eccentricity (and possibly redshift–eccentricity, or spin–eccentricity) correlations, which can be exploited in a multidimensional analysis to enhance the discriminating power of the observations. Finally, it is very likely that several different formation channels operate at the same time in the Universe. In the context of massive BHB observations, Sesana et al. (2011) studied whether *eLISA* could identify a superposition of distinct formation channels from the statistical properties of the observed population. A similar analysis in the present context is an interesting topic for future work.

ACKNOWLEDGEMENTS

AS thanks T. Dent and A. Vecchio for useful discussions. EB, AK and AN are supported by NSF CAREER Grant No. PHY-1055103. EB and AK are supported by FCT contract IF/00797/2014/CP1214/CT0012 under the IF2014 Programme. This work was supported by the H2020-MSCA-RISE- 2015 Grant No. StronGrHEP-690904. AS is supported by a University Research Fellowship of the Royal Society.

REFERENCES

Abbott B. P. et al., 2016a, Phys. Rev. Lett., 116, 241103
Abbott B. P. et al., 2016b, preprint (arXiv:1606.04856)
Abbott B. P. et al., 2016c, Phys. Rev. Lett., 116, 241102
Abbott B. P. et al., 2016d, Phys. Rev. Lett., 116, 061102
Abbott B. P. et al., 2016e, Phys. Rev. Lett., 116, 221101
Abbott B. P. et al., 2016f, ApJ, 818, L22
Antonini F., Perets H. B., 2012, ApJ, 757, 27
Antonini F., Murray N., Mikkola S., 2014, ApJ, 781, 45
Antonini F., Chatterjee S., Rodriguez C. L., Morscher M., Pattabiraman B., Kalogera V., Rasio F. A., 2016, ApJ, 816, 65
Armano M. et al., 2016, Phys. Rev. Lett., 116, 231101
Belczynski K., Taam R. E., Rantsiou E., van der Sluys M., 2008, ApJ, 682, 474
Belczynski K., Dominik M., Bulik T., O'Shaughnessy R., Fryer C., Holz D. E., 2010, ApJ, 715, L138
Belczynski K., Holz D. E., Bulik T., O'Shaughnessy R., 2016a, Nature, 534, 512
Belczynski K., Repetto S., Holz D. E., O'Shaughnessy R., Bulik T., Berti E., Fryer C., Dominik M., 2016b, ApJ, 819, 108
Benacquista M. J., Downing J. M. B., 2013, Living Rev. Relativ., 16, 4
Bird S., Cholis I., Muñoz J. B., Ali-Haïmoud Y., Kamionkowski M., Kovetz E. D., Raccanelli A., Riess A. G., 2016, Phys. Rev. Lett., 116, 201301
Breivik K., Rodriguez C. L., Larson S. L., Kalogera V., Rasio F. A., 2016, ApJ, 830, L18
Chatterjee S., Rodriguez C. L., Rasio F. A., 2016, ApJ, preprint (arXiv:1603.00884)
Cholis I., Kovetz E. D., Ali-Hamoud Y., Bird S., Kamionkowski M., Muoz J. B., Raccanelli A., 2016, Phys. Rev. D, 94, 084013
de Mink S. E., Mandel I., 2016, MNRAS, 460, 3545
Dominik M., Belczynski K., Fryer C., Holz D. E., Berti E., Bulik T., Mandel I., O'Shaughnessy R., 2012, ApJ, 759, 52
Dominik M., Belczynski K., Fryer C., Holz D. E., Berti E., Bulik T., Mandel I., O'Shaughnessy R., 2013, ApJ, 779, 72
Dominik M. et al., 2015, ApJ, 806, 263
Gerosa D., Kesden M., Berti E., O'Shaughnessy R., Sperhake U., 2013, Phys. Rev., D87, 104028
Gerosa D., Kesden M., Sperhake U., Berti E., O'Shaughnessy R., 2015, Phys. Rev. D, 92, 064016
Hartwig T., Volonteri M., Bromm V., Klessen R. S., Barausse E., Magg M., Stacy A., 2016, MNRAS, 460, L74
Kinugawa T., Inayoshi K., Hotokezaka K., Nakauchi D., Nakamura T., 2014, MNRAS, 442, 2963
Klein A. et al., 2016, Phys. Rev. D, 93, 024003
Kowalska I., Bulik T., Belczynski K., Dominik M., Gondek-Rosinska D., 2011, A&A, 527, A70
Kyutoku K., Seto N., 2016, MNRAS, 462, 2177
Mandel I., de Mink S. E., 2016, MNRAS, 458, 2634
Mapelli M., Colpi M., Zampieri L., 2009, MNRAS, 395, L71
Marchant P., Langer N., Podsiadlowski P., Tauris T. M., Moriya T. J., 2016, A&A, 588, A50
Nishizawa A., Berti E., Klein A., Sesana A., 2016, Phys. Rev. D, 94, 064020
Planck Collaboration XIII, 2015, A&A, 594, A13
Postnov K. A., Yungelson L. R., 2014, Living Rev. Relativ., 17, 13
Rodriguez C. L., Morscher M., Pattabiraman B., Chatterjee S., Haster C.-J., Rasio F. A., 2015a, Phys. Rev. Lett., 115, 051101
Rodriguez C. L., Morscher M., Pattabiraman B., Chatterjee S., Haster C.-J., Rasio F. A., 2015b, Phys. Rev. Lett., 115, 051101
Rodriguez C. L., Chatterjee S., Rasio F. A., 2016a, Phys. Rev. D, 93, 084029
Rodriguez C. L., Haster C.-J., Chatterjee S., Kalogera V., Rasio F. A., 2016b, ApJ, 824, L8
Sesana A., 2016, Phys. Rev. Lett., 116, 231102
Sesana A., Gair J., Berti E., Volonteri M., 2011, Phys. Rev. D, 83, 044036
Spera M., Mapelli M., Bressan A., 2015, MNRAS, 451, 4086
Tanay S., Haney M., Gopakumar A., 2016, Phys. Rev., D93, 064031
Wen L., 2003, ApJ, 598, 419

This paper has been typeset from a TEX/LATEX file prepared by the author.